AIP | Review of Scientific Instruments

Beam emission spectroscopy turbulence imaging system for the MAST spherical tokamak

A. R. Field, D. Dunai, R. Gaffka, Y.-c. Ghim, I. Kiss, B. Mészáros, T. Krizsanóczi, S. Shibaev, and S. Zoletnik

Citation: Review of Scientific Instruments **83**, 013508 (2012); doi: 10.1063/1.3669756
View online: http://dx.doi.org/10.1063/1.3669756
View Table of Contents: http://scitation.aip.org/content/aip/journal/rsi/83/1?ver=pdfcov
Published by the AIP Publishing

Beam emission spectroscopy turbulence imaging system for the MAST spherical tokamak

A. R. Field,[1] D. Dunai,[2] R. Gaffka,[1] Y.-c. Ghim,[3] I. Kiss,[2] B. Mészáros,[2] T. Krizsanóczi,[2] S. Shibaev,[1] and S. Zoletnik[2]
[1]*EURATOM/UKAEA Fusion Association, Culham Science Centre, Abingdon, Oxon OX14 3DB, United Kingdom*
[2]*KFKI-RMKI, Association EURATOM, P.O. Box 49, H-1525 Budapest, Hungary*
[3]*Rudolf Peierls Centre for Theoretical Physics, University of Oxford, Oxford, United Kingdom*

(Received 14 September 2011; accepted 18 November 2011; published online 23 January 2012)

A new beam emission spectroscopy turbulence imaging system has recently been installed onto the MAST spherical tokamak. The system utilises a high-throughput, direct coupled imaging optics, and a single large interference filter for collection of the Doppler shifted D_α emission from the ~2 MW heating beam of ~70 keV injection energy. The collected light is imaged onto a 2D array detector with 8 × 4 avalanche photodiode sensors which is incorporated into a custom camera unit to perform simultaneous 14-bit digitization at 2 MHz of all 32 channels. The array is imaged at the beam to achieve a spatial resolution of ~2 cm in the radial (horizontal) and poloidal (vertical) directions, which is sufficient for detection of the ion-scale plasma turbulence. At the typical photon fluxes of $\sim 10^{11}$ s^{-1} the achieved signal-to-noise ratio of ~300 at the 0.5 MHz analogue bandwidth is sufficient for detection of relative density fluctuations at the level of a few 0.1%. The system is to be utilised for the study of the characteristics of the broadband, ion-scale turbulence, in particular its interaction with flow shear, as well as coherent fluctuations due to various types of MHD activity. [doi:10.1063/1.3669756]

I. INTRODUCTION

Low-amplitude micro-turbulence driven by electrostatic, kinetic instabilities such as drift waves is thought to underlie the anomalously high transport rates observed in tokamak plasmas. These instabilities cause fluctuations in the plasma density, temperature, and potentials with a wide range of spatial scales from a few ion Larmor radii, ρ_i, down to the electron gyro-radius, i.e., $0.01 < k_\perp \rho_i < 100$, where $k_\perp$ is the perpendicular wave number of the fluctuations.[1] Efforts to characterise these fluctuations are aimed at establishing a link between the transport properties and the type of instability prevailing under particular conditions, e.g., ion or electron temperature gradient modes or trapped electron modes.[2]

The growth rates of ion-scale micro-turbulence are of order $\gamma_m \sim c_s/L_{T_i}$, where c_s is the sound speed and L_{T_i} is the temperature scale length.[3] In spherical tokamak (ST) plasmas such as in the MAST device the tangentially directed neutral beam injection (NBI) heating results in a high toroidal rotation rate ω_ϕ due to the low moment of inertia of the low-aspect ratio plasma, corresponding to Mach numbers $M_\phi = R\omega_\phi/c_s \sim 0.5$. This rotation results in strong equilibrium flow shear $\omega_{SE} \sim M_\phi c_s/L_{\omega_\phi}$, where L_{ω_ϕ} is the scale length of the rotation, which can be sufficient to suppress the growth of the ion scale turbulence,[4] when $\gamma_m/\omega_{SE} \sim$ O(1). Turbulence simulations also show that the fluctuation amplitude decreases strongly with increasing wave number $\propto k_\perp^{-\lambda}$, where λ is of order 2. This and the fact that the resulting transport rates from mixing-length estimates scale as $\gamma_m/k_\perp^2$, where γ_m is the maximum linear growth rate, imply that large scale fluctuations could potentially result in significant levels of transport. Experimental characterisation of such large scale turbulence and its dependence on the level of flow shear is hence of considerable interest for understanding the confinement of ST plasmas.

A diagnostic technique which is suited to the characterisation of large scale density turbulence is beam emission spectroscopy (BES) on heating[5] or diagnostic neutral beams.[6] The first method utilises the Doppler shifted D_α emission from the energetic deuterium atoms (typically 50–100 keV) of the heating beam, which are excited primarily by collisions with the plasma and impurity ions, and hence is approximately proportional to the local electron density. Although the heating beams are quite broad (FWHM of typically 10–20 cm) spatial localisation of the order of 1 cm can be achieved by viewing the beam in a direction parallel to the magnetic field. This is because the structure of the turbulence is "flute" like with a much longer parallel than perpendicular correlation length, i.e., $k_\perp/k_\parallel \gg 1$. By observing parallel to the field the collection volumes, which are defined by the intersection of the lines of sight with the beam, can thus be aligned to the turbulent eddies. By observing at several locations correlation analysis can be used to determine radial or poloidal correlation lengths. With multi-channel detectors imaged at the plasma with a radial (or poloidal) separation of 2 cm, fluctuations with wave-numbers $k_{r,\theta} < 1.6$ cm^{-1} can be resolved, corresponding to $k_{r,\theta}\rho_i < 1$ for $\rho_i \sim 0.7$ cm typical of MAST plasmas. By extending the observations to two dimensions using an array of detectors it is also possible to image the density fluctuations.[7] This paper describes such a BES turbulence imaging system which has been recently implemented on the MAST device.

The availability of 2D images of the ion-scale density turbulence allows the study of detailed physics of plasma transport. As well as determining correlation times and correlation lengths in poloidal and radial directions, velocimetry using a time-delay correlation method allows the poloidal propagation of turbulence to be determined. This information has allowed study of the influence of sheared mean poloidal flows on formation of internal transport barriers on DIII-D.[8] The ability to detect fluctuating poloidal flows has also enabled detection of zero mean frequency zonal flows and Geodesic-Acoustic-Modes[9] from such 2D BES data, which are thought to be involved in the self-regulation of the turbulence. Techniques used in other fields for image analysis have also been applied to determine the 2D flow field of the turbulence[10] which could then be used to determine the turbulent particle flux or Reynolds stress. Application of techniques used for analysis of phase contrast imaging (PCI) measurements on the Large Helical Device (LHD) (Ref. 11) could also be applied to such data to determine the 2D k-spectrum using Maximum Entropy methods.

A further requirement on the observation geometry is to view with an appreciable component colinear with the beam. This provides both an increase in the intersection length with the beam and, most importantly, large Doppler shifts (typically 1–3 nm) of the D_α emission from the beam atoms, which is an essential requirement to separate the beam emission from the much more intense passive D_α emission from the plasma boundary. By availing of high étendu optics to collect sufficient photons and relatively simple optical technology, i.e., interference filters and solid-state detectors, it is possible to achieve adequate signal-to-noise ratio (SNR) to measure relative density fluctuations of order 0.1% over the 0.5 MHz analogue bandwidth.

This paper describes the technical realisation of the BES turbulence imaging system on MAST. The conceptual design of this system is based on simulation calculations, which were presented in an earlier paper.[12] These were used to determine the achievable signal-to-noise ratio and hence the sensitivity in terms of minimum relative density fluctuation level $\delta n_e/n_e$ at a given sampling rate. These calculations were benchmarked against the measured performance of a trial 8-channel BES system which was implemented on MAST, which utilised the collection optics of the CXRS system.[13] In Sec. II, the fundamental design considerations are described, including the choice of viewing geometry, detector, optical system, and estimates of the sensitivity in terms of the detectable density fluctuation level and the spatial resolution. In Sec. III the optical design of the system is described as well as the technical realisation of the optical hardware on the MAST tokamak. Section IV describes the custom avalanche photodiode (APD) array camera on which the design of the system is based. In Sec. V initial results from the BES system are presented, including spectral measurements from which the ratio of beam emission signal to background is estimated and compared with the spectrally integrated beam emission signals. Initial results are also presented which demonstrate some basic characteristics of the broadband turbulence and also detection of coherent MHD mode activity. A summary and some initial conclusions from this work are presented in Sec. VI.

II. DESIGN CONSIDERATIONS

There were some external engineering constraints on the design which had to override any other considerations. Firstly, the provision of any new ports in the MAST vessel was prohibited because these would compromise the strength of the vessel in view of a planned upgrade to the device. The BES system therefore had to make use of an existing port, which necessitated the implementation of a periscopic collection optics located inside the UHV vacuum envelope. It was also decided at a relatively early stage in the project to make use of a custom camera system based on an 8×4 channel APD array sensor (Hamamatsu S8550) imaged at the beam location with direct coupled optics instead of using optical fibre coupling.

The relatively large number of channels (32) of the APD array together with the necessity for high étendu optics would have required several large diameter optical fibres per channel to achieve the same performance. With an *f*-number of 1.2 at the detector and an active area of each pixel of 1.6×1.6 mm^2 the resulting étendu is $\sim 1.1 \times 10^{-6}$ m^2 sr pixel^{-1}. To achieve this with 1 mm diameter optical fibres illuminated at F/2 would require at least 8 fibres per channel, hence requiring almost 8 km of fibre altogether. On the other hand there are some disadvantages with the direct coupled optics. Firstly, the spatial arrangement of the channels at the plasma is fixed, whereas with fibres it is relatively simple to re-arrange the viewing geometry. The size of the detector image and hence channel separation also varies with the distance from the collection optics to the viewed location at the beam. Furthermore, with the APD detectors located in the vicinity of the tokamak, if the NBI power is increased for a future upgrade, interference from beam-thermal D-D neutrons or hard x-rays detected by the APDs may require addition of some neutron shielding of the detector.

A. Viewing geometry

In order to optimise the spatial localisation of the measurement the line of sight has to be oriented along the magnetic field where it intersects the heating beam. Because the turbulent fluctuations are elongated along the field, i.e., $k_\perp/k_{||} \gg 1$, this minimises the spatial averaging within the emission volume over the fine scale fluctuations in the direction perpendicular to the field. As discussed in Ref. 12, for co-beam directed (red-shifted) views, the optimal viewing locations lie along an almost vertical locus at the vessel wall at a toroidal location about -38° toroidally displaced from the beam port. Moving outwards from the magnetic axis the optimal location for the collection optics shifts from the mid-plane to a vertical position $\sim$1 m below the mid-plane, hence for a fixed optics, the view is optimal at a particular plasma radius. Other constraints, i.e., the in-vessel (P5) poloidal field coils above and below the mid-plane in MAST, restrict the location of the viewing optics to a position 0.4 m below the mid-plane or above. With the optics at this location the view is optimised for a major radial location of 1.2 m (corresponding to a normalised radius $r/a \sim 0.5$) for a typical MAST toroidal field and plasma current (800 kA, 0.48T). A schematic of the viewing geometry is shown in Figure 1.

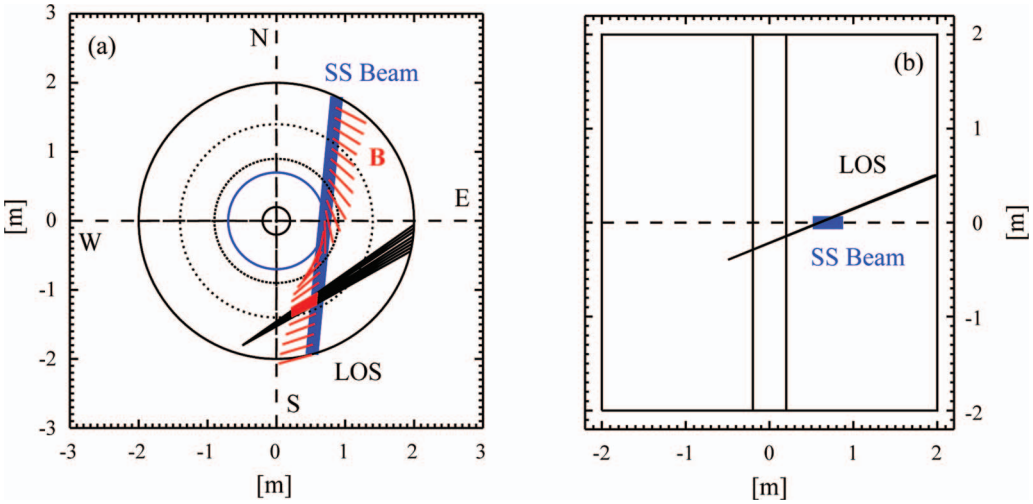

FIG. 1. (Color online) Plan and E-W sectional view of the observation geometry of the BES imaging system. The direction of the magnetic field vectors are indicated at several locations along the path of the SS beam. The inner and outer dotted circles show the locations of the magnetic axis and the outboard plasma edge respectively and the solid circle the beam tangency radius.

An available NW160 port (HM-07) located one sector clockwise (30°) from the SS beam port was selected for the BES system, hence the viewing location is misaligned toroidally by ∼8° from the optimal location. Through this port pass both the optical path and actuators for scanning the viewing location and a shutter mechanism, hence, a smaller NW63 window had to be used for the optical path. The centre of the NW160 port was located 0.2 m below the mid-plane, with the NW63 window offset vertically upwards in the larger flange.

In order to maximise the SNR, the collection optics should have as large an aperture as possible. However, the aperture should not be so large as to degrade the spatial resolution due to the finite size of the collection cone within the emission volume along the intersection depth of the line-of-sight with the beam of ∼20 cm. The maximum acceptable aperture at the collection lens of F/10 is determined by matching the cone size to the spatial smearing due to the line-of-sight integration through the beam and the curvature of the B-field. Using the simulation calculations described in our earlier paper,[12] when viewing the beam from a PINI type NBI source on MAST, this spatial delocalisation is estimated to be ∼2–3 cm, increasing with the observed radius. With a nominal distance to the beam of ∼1.4 m for a viewed radius of 1.2 m this requires a collection lens of 140 mm diameter.

More detailed calculations of the spatial response of the 2D BES system are presented in Ref. 14, which describes calculations of the point-spread functions (PSF) and spatial transfer functions (STF) taking into account relevant physical effects, including the finite lifetime of the excited atomic state. Such data are required to generate synthetic turbulence data from results of numerical turbulence simulations for direct comparison with observations.

B. Optical system

In Figure 2(a) a schematic of the optical system used for the BES system is shown. A periscope arrangement consisting of a plane, elliptical collection mirror (M1, 140/200 mm diameter) and a second deflection mirror (M2) provide the vertical offset between the location of the window and the viewing location. A fused-silica doublet collection lens (L1, 140 mm diameter) produces an image of the beam with a nominal factor ∼5 de-magnification just inside the window. This allows the light to pass through the relatively small aperture window. The overall magnification of the optics is chosen to match the pixel separation of the detector (2.3 mm) to a 2 cm channel separation at the beam for a nominal viewing radius of 1.2 m, i.e., by a factor 8.7. With the 8 × 4 array detector this results in a spatial coverage of 140 mm horizontally and 60 mm vertically between channel centres.

A field lens (L2) located at the intermediate image couples the light through the window to a second pair of imaging lenses (L3) outside the window. These form a 1:1 image of the beam at a pair of field lenses (L4, 180 mm diameter) arranged to form a region between where the rays are tele-centric, i.e., the principle rays across the image are parallel. This and the narrow F/10 aperture results in a narrow range of incident angles ($\theta_{max} \sim 3°$) at the large rectangular (170 × 90 mm^2 full aperture) interference filter (F1) which is located between these field lenses. This is required in order to minimise the spectral broadening of the filter bandpass due to the finite range of incident angles in the incident light cone.

The optics is completed by a deflection mirror (M3) (deflects light into the picture in Figure 2), which allows for convenient alignment of the optical axis, and a final

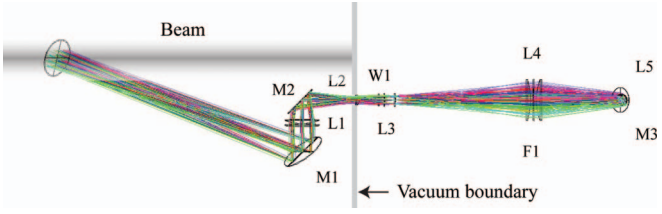

FIG. 2. (Color online) Optical layout of the 2D BES imaging system produced by ZEMAX ray tracing program. Note that lens L5 and the detector are behind mirror M3, i.e., M3 deflects the beam into the paper.

imaging lens (L5). This final lens is a large aperture, commercial Nikkor (F/1.2, 50 mm) camera lens, which forms an image at the APD sensor. The focussing ring on this lens can be used to alter the effective focal length of the optical system and hence focus the sensor at different distances from the collection optics. Different radial locations in the plasma can be viewed by scanning the viewing location along the beam axis, at major radii at the centre of the array ranging from 0.9 m at the magnetic axis to 1.5 m at the outer plasma edge. Over this range the magnification of the optics and hence the inter-channel separation at the beam changes, by a factor of 1.2–0.86 respectively relative to that at a nominal viewed radius of 1.2 m. The focusing of this lens is performed remotely using a stepping motor drive.

The viewing location is scanned along the beam between discharges by rotating the collection mirror M1 about a single, near-vertical axis, which is normal to the plane containing the mirror centre and the beam axis. A consequence of this is that the image of the beam at the filter and the detector rotates around the optical axis as the mirror is rotated. This necessitates rotating both the rectangular filter to avoid vignetting of the outer channels and the APD camera to orient this to the beam axis. The mechanics of the rotation of the mirror, filter and camera is described in detail in Sec. III.

C. Predicted spectra

The angle between the line-of-sight and the beam varies between 40° and 60° when viewing locations at the magnetic axis or the plasma edge, hence, there is a change in the Doppler shift due to the variation in the projection of the beam atom velocity along the line of sight. For a deuterium (D^0) beam with 75 keV energy, the range of Doppler shifts of the D_α beam emission is 2–3 nm to the red side of the unshifted background D_α line at 656.1 nm. Figure 3 shows spectra for the spectral region of relevance for the BES measurements produced by the simulation code[12] for NBI energies of 75 keV and 60 keV. The intensities of the beam emission components are calculated absolutely, while the background D_α and CII line intensities are matched to measured spectra. It can be seen that the full and half-energy beam emission components (E_0, $E_0/2$) are separated from the neighbouring CII lines but the third energy componets ($E_0/3$) are not. The bandpass of a single interference filter of central wavelength λ_0 of 660.2 nm and full-width-half-maximum ($\Delta\lambda$) of 2.0 nm is superimposed. It can be seen that this single filter can encompass the full-energy beam emission components from the full radial range at the 75 keV beam energy, while rejecting the CII lines which lie outside the 10% transmission range of the filter. At the lower beam energy the full-energy components from the outermost locations are quite strongly attenuated. Under these conditions the signal-to-background ratio of the measurements is hence degraded as discussed in Sec. V A.

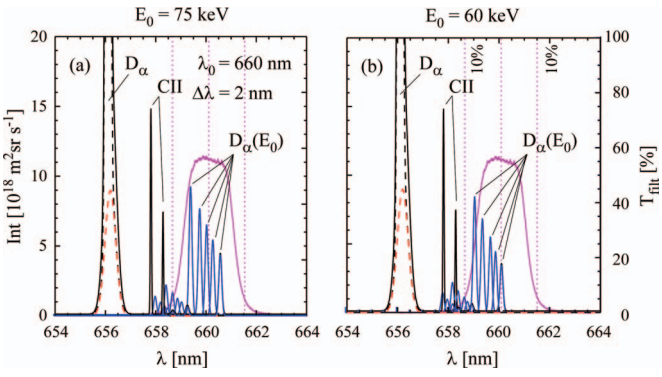

FIG. 3. (Color online) Predicted spectra for beam energies of (a) 75 keV and (b) 60 keV. The total emission is shown for a viewing radius of 0.9 m, with the contribution to the D_α beam emission from the three energy components for viewing radii of 0.9, 1.0, 1.1, 1.2 and 1.3 m superimposed. The transmission of the interference filter is also shown. The vertical dashed lines are the 10% transmission wavelengths and the central wavelength of the filter.

D. Interference filter

It was decided to use a single interference filter located at the intermediate 1:1 image for all of the spatial channels. A three-cavity, rectangular filter of 170 × 90 mm^2 size was obtained from Andover Corp. at a reasonable cost and was supplied un-mounted as a trial. The specification of the filter was for an out-of-band blocking from FIR to x-ray of 10^{-4} and bandpass with central wavelength λ_0 of 660.2 (+0.4, −0.0) nm, bandwidth (FWHM) $\Delta\lambda$ of 2.0 ± 0.5 nm over a useful area of the filter of 160 × 80 mm^2 and a peak transmission of the filter of at least 45%. With an effective refractive index of 2.05, illumination at F/10 results in an average shift of the bandpass to the blue by 0.2 nm. Superimposed on the spectra in Figure 3 is the measured bandpass for a channel near the middle of the actual filter. The achieved peak transmission of the filter was 57%.

The interference filter is of a particularly large size hence control of the filter tolerances over the peripheral regions of the filter during manufacturing was challenging. In Figure 4, the bandpass characteristics are shown as determined from the bandpass functions measured at 32 locations over the surface of the filter at 2 cm horizontal and vertical (Δx and Δy) spacing. A collimated beam of white light with a beam diame-

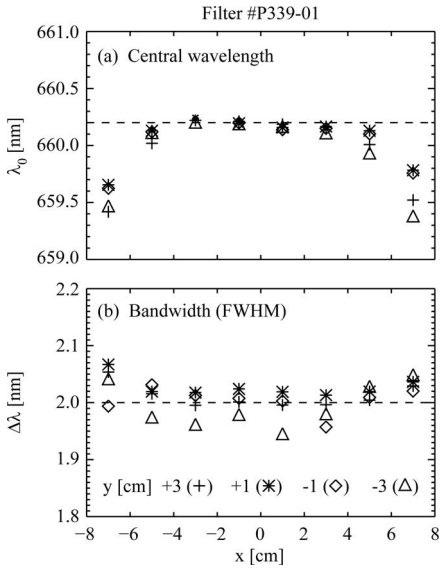

FIG. 4. Measured bandpass characteristics at 32 locations over the surface of the BES interference filter corresponding to the BES spatial channels: (a) central wavelength λ_0 and (b) bandwidth (FWHM), $\Delta\lambda$.

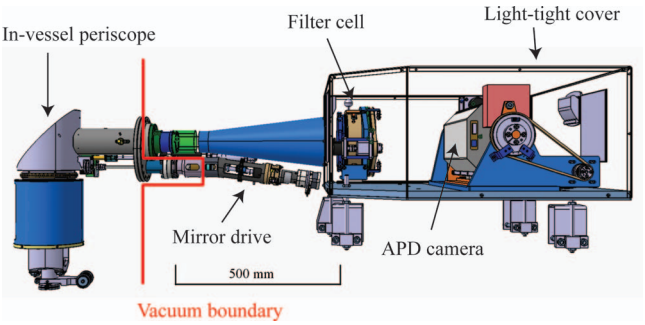

FIG. 5. (Color online) Overview of the complete BES imaging system (the vacuum boundary is indicated by the vertical line).

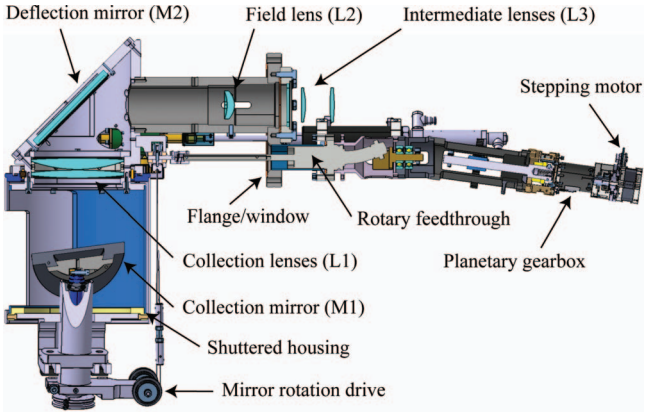

FIG. 6. (Color online) Sectional view of the in-vessel collection optics.

ter of 2 cm was used to illuminate the filter for these measurements. It can be seen that the full-width-half-maximum (FWHM) bandwidth $\Delta\lambda$ of the filter is well controlled over the full aperture within a deviation of ± 0.05 nm which is much smaller than the quoted tolerance. There is however an appreciable shift of the central wavelength λ_0 at the two ends of the filter corresponding to columns 1 and 8 of the 2D array. This shift is about -0.5 nm for the middle two rows (2 and 3) and largest at about -0.8 nm for the locations in the outer corners (rows 1 and 4). As discussed in Sec. V A this shift of the bandpass to shorter wavelengths at the ends of the filter results in greater level of background from the CII (658.3 nm) line, for which the transmission is $\sim$20% for the corner channels compared to 1% or less for the other more central channels.

III. OPTO-MECHANICAL SYSTEM

The technical realisation of the BES opto-mechanical hardware is described in detail in Ref. 15. An overview of the BES hardware is shown in Figure 5. This consists of the in-vessel periscopic collection optics, which is mounted from a support tube on the inside of the NW160 vacuum flange, the associated drives for the mirror rotation and a shutter mechanism on the outside of the flange and the external optical components on a separate base plate. A stringent constraint on the design was that the periscope assembly had to fit in the 260 mm gap between the vessel wall and the P5 coil case. Also, the footprint of the hardware immediately outside the port had to be as small as possible to accommodate other surrounding diagnostic hardware. In order to minimise perturbation to the magnetic field of the tokamak, non-magnetic materials were used where possible and for the in-vessel components all materials had a relative permeability of 1.05 or less.

A. In-vessel collection optics

A schematic of the in-vessel periscopic collection optics is shown in Figure 6. Looking back along the light path, the principle light ray is incident vertically at the collection mirror, which is tilted to reflect the light to cross the axis of the beam. The viewed location along the beam can be scanned by rotating the mirror about a single axis which is tilted from the vertical so that it is normal to a plane through the center of the mirror and the axis of the beam. This is achieved by mounting the mirror bearings on a curved track below the mirror which allows adjustment of the mirror tilt about its centre. This track can also be rotated about a vertical axis to align it with a vertical plane joining the mirror centre with the nearest point along to the beam path. The alignment of the mirror axis has only to be made once during installation. The bearings of the rotation axis are full ceramic to prevent seizure under UHV conditions. The mirror mount is attached to a support tube, which also serves as a protective cover for the mirror. This tube is mounted below the body of the periscope which houses the collection lens cell, shutter bearing and deflection mirror and is attached to the flange by a support tube through which the light passes.

A shutter is provided to protect the mirror during glow-discharge cleaning of the vessel between plasma shots. This shutter is in the form of a shell with an aperture which rotates around the lower support tube in which there is a similar aperture. The shutter is operated by a pneumatic cylinder via a linear UHV feedthrough.

The actuator for the rotation of the mirror is a stainless-steel wire loop running over a lower pulley attached to the mirror axis, around two guide rollers and an upper pulley. The upper pulley is rotated by means of a stepping motor, via a 16:1 reduction gearbox and a rotatary UHV feedthrough. There is an overall reduction ratio of 48:1 from the motor to the mirror rotation. A relative encoder is attached to the drive shaft and end switches are provided which provide an absolute reference for the mirror position. In laboratory tests, an overall positional accuracy of better than ± 3 mm at the beam was achieved, corresponding to an angular accuracy of $\pm 7'$.

The elliptical collection mirror and the deflection mirror are manufactured from stainless-steel coated in silver and over-coated with a reflection enhancing layer of SiO_2. The reflectivity of the mirrors is 98% at 650 nm. The collection lenses are of fused silica with a hard, anti-reflection coating optimised for 650 nm. All of the stainless steel components are of SS-316-L. PEEK (poly-ether-ether-ketone) is used for the roller bearings and phosphor bronze for the wire pulleys to avoid seizure under UHV conditions.

B. Ex-vessel detection optics

The intermediate lenses (L3) are mounted in a cell on the outside of the flange. The light path to the ex-vessel optics

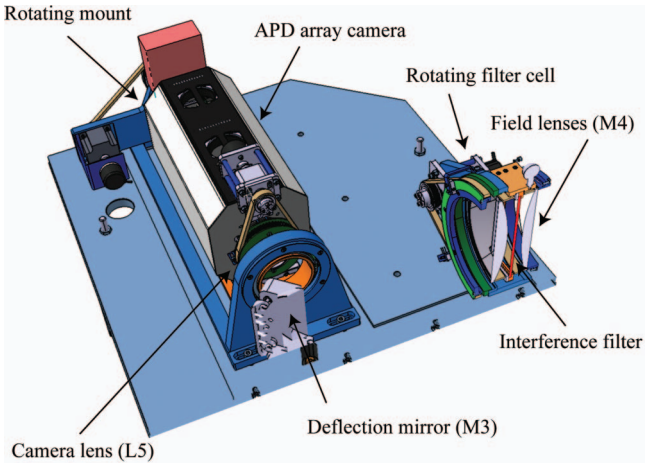

FIG. 7. (Color online) Schematic of the ex-vessel optical hardware.

is enclosed by a light-tight cone, which allows for movement of the MAST vessel during baking. The ex-vessel optics consisting of the field lenses (L4), filter (F1), deflection mirror (M3), APD camera, and imaging lens (L5) are mounted on a base plate, as shown in Figure 7. The deflection mirror allows for adjustment of the optical axis to the APD camera. As explained above, the rotations of the filter cell and the APD camera, which are required as the radial position is scanned, are performed using stepping motor drives. End-switches and relative encoders provide an absolute position reference and measurement. The camera lens (L5) can also be focussed remotely using a stepping motor to adjust the focal position at the beam. The ex-vessel optics has a light-tight cover, the removal of which is interlocked with the power supply for the APD camera to protect the sensor from over exposure.

IV. APD CAMERA SYSTEM

A. Overview

The detection system is based on the Hamamatsu S8550, 4 × 8 channnel APD array sensor which is integrated into a custom camera system. This APD camera (APDCAM) system was designed and manufactured by ADIMTECH Ltd (ADIMTECH Kft., Konkoloy Thege Miklós út 29-33, Budapest 1121, Hungary), a spin-off company of RMKI/KFKI institute of the Hungarian Academy of Sciences. The system integrates the sensor, pre-amplifier, ADC board with field programmable gate array (FPGA) to perform triggering, data manipulation and buffering functions, HV power supply, control of detector temperature, calibration light and electromechanical shutter, and Ethernet communications into a compact package.

B. Detector choice

The choice of optimal detector for this high-bandwidth and low-light level application is discussed in detail in Ref. 14, as is the design of the pre-amplifier electronics. At the expected level illumination of $\sim 10^{11}$ photons/s, the APD detector offers the optimal SNR and flexibility. At lower light levels, photomultiplier tubes (PMTs) are the optimal choice due to their high (up to 10^7) intrinsic gain and relatively low-noise. This results in a high output signal (from μA to mA), which hence obviates the need for special amplifier electronics. This means that the SNR is very close to the photon statistical limit calculated with the detected photon flux. The disadvantage of PMTs is their low QE (<10%) and high sensitivity to stray magnetic fields.

At higher light levels, photoconductive photodiodes (PPDs) are most suitable due to their high QE, which in the 650–670 nm region is as high as 85%. The PPDs do not have intrinsic gain, therefore, even at a quite high photon flux, their signal is very low (10^{10} photons/s $\sim$ 1.5 nA), hence requiring use of Peltier or cryogenically cooled state-of-the-art amplifier and read out electronics. These detectors are also insensitive to magnetic fields. The QE of APDs are similarly high; however, the APD multiplication process introduces additional (excess) noise, which can be expressed as a reduction of the effective QE to values of typically 40%. Nevertheless, in a certain photon flux range, the SNR of the APD will be higher than that of the PPD. The gain of the APD and the dark current are temperature dependent, therefore, they should be temperature stabilized but they do not need to be operated at cryogenic temperatures.

The Hamamatsu S8550 sensor integrates 32 sensors of 1.6 × 1.6 mm^2 sensitive area at a pitch of 2.3 mm into a single package as shown in Figure 8. The detectors share a common anode to which a bias voltage in the range 200–390 V is applied, resulting in an intrinsic gain in the range 2–100. The QE peaks at 85% at 650 nm which is optimal for this application. The detector is in contact with a copper tab which is heated or cooled using a Peltier element to stabilise the temperature to a set point in the range 10–30 °C. The camera housing has a Nikon F-mount for a lens behind which is a BK7 glass window and an electromagnetic shutter. The camera integrates control of the shutter, sensor temperature and the HV supply. A calibration light source is also incorporated into the camera housing in the form of a high-intensity red LED coupled to the sensor using fibre optics. This facilitates testing of the detector electronics and measurement of the noise spectrum at the same light level as in the experiments.

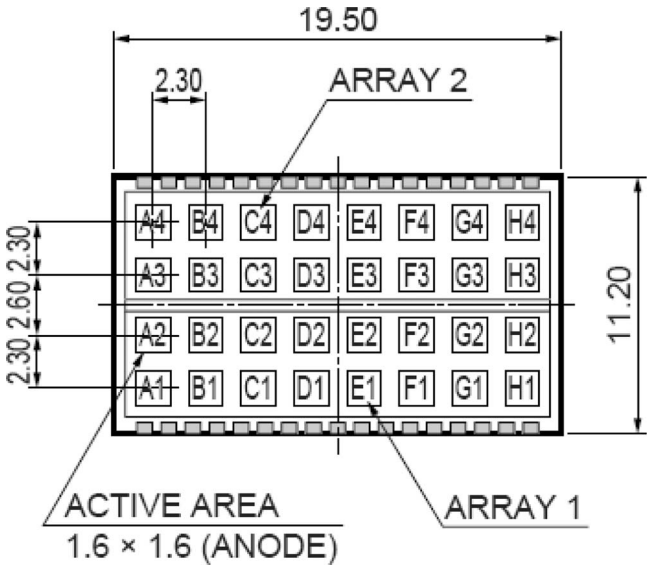

FIG. 8. Dimensions of the Hamamatsu S8550 APD array sensor.

C. Pre-amplifier

The design of the pre-amplifier is also discussed in detail in Ref. 16. There are currently two versions with different bandwidths with −3 dB points of either 0.5 MHz or 1 MHz. The 0.5 MHz version is used for the measurements presented here. The amplifier consists of a current to voltage converter followed by a further gain stage. The current to voltage converter is based on an AD8065, ultra-low noise, high bandwidth FET input operational amplifier, which has extremely low input voltage and current noise of 7 $\text{nV}/\sqrt{\text{Hz}}$ and 0.6 $\text{fA}/\sqrt{\text{Hz}}$, respectively. The amplifier stage consists of a high-performance, low-noise, high gain-bandwidth-product ADA4899 operational amplifier (0.6 GHz at −3 dB with unity gain), which is currently set up to operate with a gain of 50. Offset compensation is incorporated between the first and second stages of the pre-amplifier to correct for any amplifier offset and detector dark current. The offset voltage can be set using DACs for each channel independently. The pre-amplifiers for each of the 32 APD channels are integrated into a single multi-layer PCB with surface mount technology onto which the sensor is mounted.

D. Digital electronics

The data acquisition unit incorporates four 8-channel 10–50 MHz, 14-bit AD9252 ADCs, and a Xilinx Virtex-5 FPGA which implements clock and trigger functions, digital low-pass filtering, re-sampling and buffering of the data, which is packed into UDP packets and output to the 1 Gbit Ethernet controller. The controller transmits the data to the host PC via a fibre optic connection. The ADCs function all of the time but the data are only transmitted in response to either an internal or external trigger, allowing various triggering modes to be implemented. The data from the ADCs is filtered using a FIR digital, low-pass filter with a steep cut-off just below the required sampling frequency. An additional recursive filter is implemented to allow for a lower cut-off frequency with a less steep characteristic. After the filtering the output resolution is selected at 8, 12, or 14 bits. The data are then re-sampled at lower frequency defined either by an external clock or a divided version of the internal 20 MHz clock. The down sampled (decimated) data are then stored in a ring-buffer with up to 1024 samples per channel, which allows pre-triggering functions to be implemented. The triggers are common to all 32 channels and can either be an external TTL signal or generated internally. Data transmission commences after waiting for a pre-programmed delay of up to several 10 s. An internal trigger can also be generated in response to a condition that any one of the 32 input channels fulfils a trigger condition, i.e., the signal level is above or below a set threshold. This facility together with the ring-buffer is particularly useful in pre-triggering in response to fast transient events. The bandwidth of the 1 GBit Ethernet link is sufficient to transmit 32 channels at 14-bit resolution at 2 MHz sampling rate. The data streams are written directly to the memory of the host PC, hence the measurement time length is limited by the computer memory.

E. Performance

Using the simulation code it is possible to calculate the incident photon flux at the detectors and hence the expected signal level from the APD detectors. With the PINI NBI source operating at 1.8 MW and 60 keV energy, the simulated incident photon rate at the detectors is $\sim 2.2 \times 10^{11}$ s^{-1} at an observation radius of 1.2 m in the L-mode discharge #17068 (as used for the simulation calculations for the trial BES system[12]). This is two orders of magnitude larger than for the trial BES system observing the SW beam from the ORNL source at 1.2 MW and 48 kV energy. This is a consequence of the increased collection etendu and also the higher beam energy of the PINI source.

The APD camera pre-amplifier has a load resistor R_L of 68 kΩ and a second-stage gain of 50. (This compares to values of 50 kΩ and 100 respectively for the trial BES detectors.) The resulting sensitivity S_V expressed in terms of the transimpedance is 3.4×10^6 V/A. For the APD bias voltage of 290 V, as used for the measurement of discharge #26086 presented in Figure 10, the APD gain is ∼5 at which the excess noise factor is ∼1.4. The corresponding output voltage of the APD camera for the simulated case for #17068 is hence ∼0.6V with a SNR of ∼200. This compares to the SNR achieved with the trial system of order ∼10.

With the un-illuminated sensor at a bias voltage of 310 V, the measured rms noise level from the electronics at the ADC input is ∼2.2 mV. This is compared to the photon noise level at the typical signal levels for measurements in Sec. V B. The local magnetic field from the tokamak is a horizontal component from the nearby toroidal field coils of ∼10 G and a vertical field of ∼50 G. Only the latter produces a barely discernable signal due to pickup of ∼0.5 mV amplitude and is hence negligible.

V. INITIAL RESULTS

A. Spectral measurements

In order to assess the quality of the spectrally integrated D_α beam-emission (BE) data it is necessary to determine the ratio of BE intensity (which is localised to the intersection volume of the line-of-sight and the beam) to the background emission. The background is from several sources: the CII (657.81, 658.29 nm) doublet lines, broadband emission from bremsstrahlung, the D_α emission from secondary neutrals due to charge exchange with the fast-ions from the beam (FIDA signal) and possible contributions from molecular emission and other weaker spectral lines. The CII emission is from a region near the plasma edge a few cm in radial extent but is distributed over the whole plasma surface rather than being localised to the beam. Because this emission is proportional to the plasma density it will augment the BES fluctuation measurements when observing near the plasma boundary but confuse the measurement when trying to detect core plasma turbulence of lower relative amplitude. The bremsstrahlung emission is predominantly from the plasma core $\propto n_e^2/\sqrt{(T_e)}$ but is distributed along the line of sight rather than localised to the beam. The bremsstrahlung intensity is estimated to be less than 1% of the BE intensity for typical conditions.

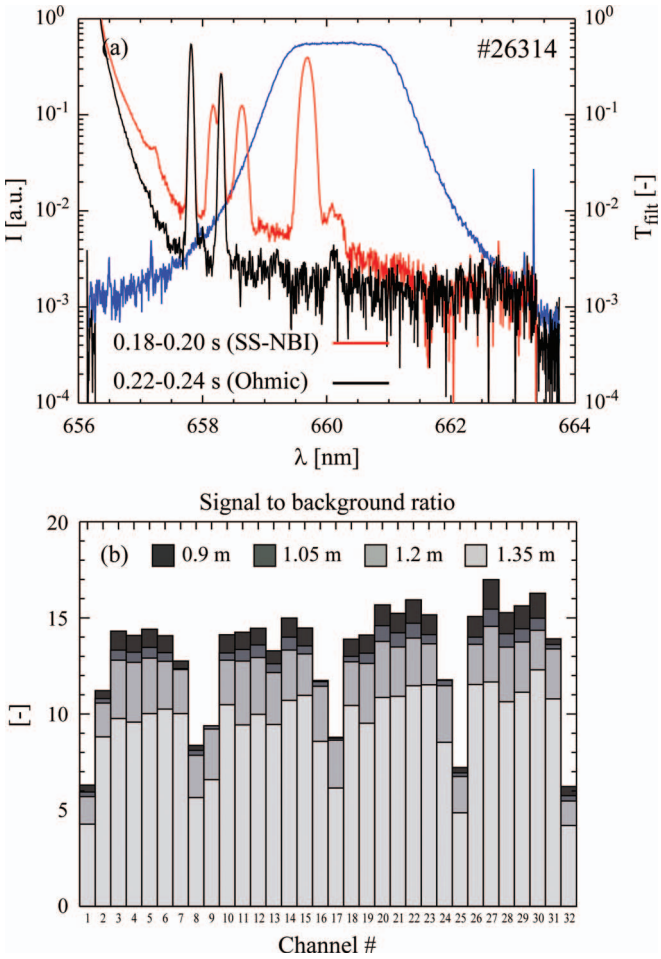

FIG. 9. (Color online) (a) Spectra measured both before and after the SS beam cut-off time using the MSE spectrometer at a view radius Rv of 1.2 m together with the transmission of the BES filter and (b) the ratio of BE signal to background estimated from the spectrally integrated intensity during the periods with/without the beam for each spectral channel.

In Figure 9(a) spectra are shown measured from the mid-plane at the same toroidal location as the BES collection optics using the optics of the Motional-Stark-Effect (MSE) diagnostic viewing at a radial location R_m of 1.2 m. The observed Doppler shifts of the D_α BE lines will be almost the same as those for the BES system which is located 0.4 m below the mid-plane. Spectra are shown during a period with the SS beam at 62 keV injection energy and during the ohmic phase just after the beam is switched off. By integrating the spectra under the filter bandpass function measured at the location of each of the 32 spatial channels on the filter the spectrally integrated intensity during (I_{SS}) and after (I_{OH}) the SS beam cut-off can be determined. The ratio of BE signal to background (SBR) can then be calculated from $SBR = (I_{SS} - I_{OH})/I_{OH}$. This is plotted for each spatial channel in Figure 9(b), where the channel numbering is in row-column order across the filter (row 1, channels 1–8, etc). As discussed in Sec. III B, due to the large size of the filter there is some broadening of the bandpass at the outer extremes, i.e., for columns 1 and 8. For these channels more of the CII emission is detected and the modelled SBR is reduced to the range 5–10. For the more central channels the SBR is higher in the range 10–15. These values are compared to the SBR estimated from the evolution of the BE signal at a beam cut-off as discussed in Sec. V B below.

The transmission of the filter at the wavelengths of the CII (657.81, 658.29 nm) lines is ~0.04% and 0.3% for the central channels and somewhat higher for the four corner channels at 0.08% and 2%. By cutting out these lines from the spectra shown in Figure 9(a) it is possible to calculate the fraction of the background due to these CII lines as ~10% for the middle channels and ~50% for the corner channels. Another source of background emission is hence dominating the background for most of the channels. As mentioned above, bremsstrahlung can account for only ~10% of the background emission at moderate densities and the *SBR* is also found not to have any clear dependence on density, supporting this conclusion.

The transmission of the filter as a function of wavelength is also shown in Figure 9(a). At the wavelength of D_α (656.1 ± 1.0 nm) the average transmission is 1.0% for the middle and 15% for the corner channels. The D_α emission has a warm component from charge exchange neutrals and also the FIDA component. Using the part of the spectrum at wavelengths greater than 657 nm to exclude any contribution from the D_α intensity at shorter wavelengths, for the middle channels the SBR increases from ~15 to ~20 indicating that about 30% of the background intensity is due to D_α. For the corner channels this contribution increases to ~75%.

Although the SBR is typically in the range 10–15 it is found to be highly variable, the background light sometimes increasing to result in a SBR low as ~3. Very recently, spectral measurements were made through the BES optics by replacing the APD camera with optical fibres at the image plane of the camera objective. These measurements showed that the origin of this excessive background light was D_α light passing the rectangular interference filter through the outer regions of the circular field lenses which were not blocked by the filter. Although these regions are not imaged directly onto the detector, there is sufficient scattering of the intense, passive D_α emission (which is two orders of magnitude brighter than the beam emission) within the objective lens for this scattered light to be a significant fraction of the detected beam emission intensity. By masking these outer regions of the field lenses the background light level could be reduced by a factor ~5, resulting in a corresponding increase in the SBR to ~50. These modifications now allow for considerably improved measurements of the core turbulence characteristics than were possible before.

B. Initial BES measurements

The evolution of the spectrally integrated signals from the BES system is shown in Figure 10(e) for a MAST discharge in which the SS beam was injecting ~1.5 MW of D^0 at 62 keV energy from 0.05 to 0.2 s. The discharge was a 790 kA plasma current, L-mode discharge with a double-null diverted (DND) magnetic configuration with line average electron density increasing during the shot to about 4×10^{19} m^{-3}. The BE signals increase slowly after starting the SS beam because the plasma radius at the outboard mid-plane was increasing during the early phase and is initially inside the observed radial

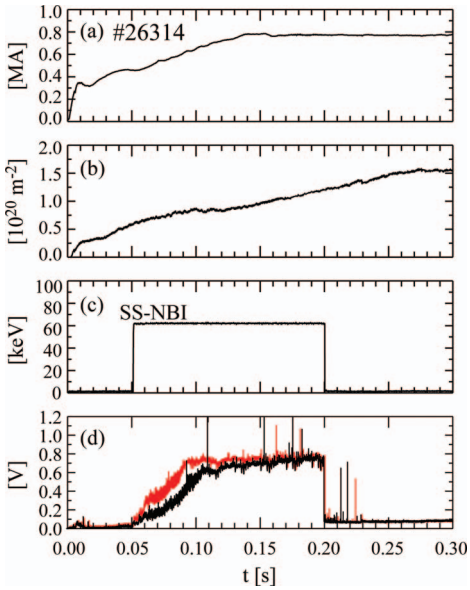

FIG. 10. (Color online) Evolution of (a) plasma current, (b) line-integrated electron density, (c) SS beam injection energy E_0, (d) SW beam injection energy; and (d) BE signals from channels 13 (upper trace) and 16 (lower trace) in the frequency band from 0 to 50 kHz.

location. The magnitude of the signals of 0.8 V corresponds to an incident photon flux at the APDs of $\sim 3.4 \times 10^{11}$ s^{-1} assuming an APD gain of ~5 at the bias voltage of 290 V. This output voltage is in reasonable agreement with the prediction of the simulation calculations discussed in Sec. IV D. The centre of the array was viewing a major radial location $R_v \sim 1.2$ m with the channels 13 and 16 viewing locations at 1.19 and 1.13 m radius and nominally 1 cm below the midplane. The locations of the magnetic axis and the outboard separatrix were at 0.97 and 1.4 m during the constant current phase of the discharge, hence the observation locations are in the mid-radius, gradient region of the plasma.

The BE intensity I_{BE} is proportional to the product of the beam density n_b and the electron density n_e ($I_{BE} \propto n_b n_e$), hence the relatively constant intensity during the density ramp implies that the increasing density is compensated by an increase in the beam attenuation at the observed location. At the same bias setting and viewing radius, discharges with the SW beam only exhibit a barely discernable ~10 mV drop in the BE intensity at the switch-off time of SW beam, indicating that the system does not detect a significant signal from this beam. At the time of SS beam cut-off, the BE signal decreases from ~0.8 V to ~0.08 V, i.e., by a factor ~10 in both channels 13 and 16. This is to be compared to the modelled SBR shown in Figure 9(b), which is calculated from the measured spectrum, for the channels 13 and 10, respectively. Note that after masking out the light passing by the interference filter, the background light level was reduced by a further factor ~5.

Some background signal is produced by neutron, gamma or hard x-ray radiation detected by the APDs, the latter produced only when there are runaway electrons. This is in the form of sharp spikes in the signal with significant amplitude only over 3–4 samples as a result of the 0.5 MHz amplifier bandwidth. These peaks are uncorrelated between channels and result in a broadband, white noise contribution to the signal which adds to the photon noise level. The mean signal level due to these pulses is insignificant compared to the electronic noise level of ~0.5 mV. The typical pulse rate due to radiation is 1000 s^{-1} per channel which represents only about 0.5% of the digitized samples. A numerical algorithm is used to remove these peaks based on their known temporal structure, which is activated once the amplitude of the high-pass filtered signal exceeds a threshold voltage. For threshold voltages of 10 mV or less there is no further reduction in the broadband noise floor of the data, indicating that this radiation background has been effectively removed by this procedure.

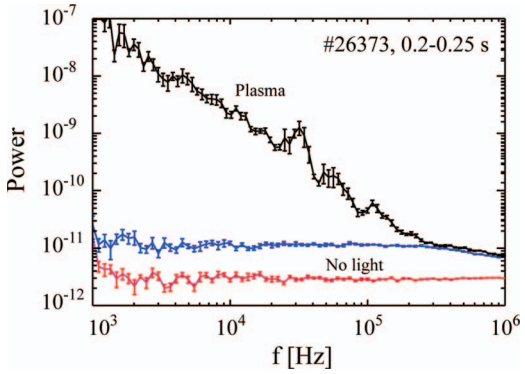

FIG. 11. (Color online) Comparison of signal power as function of frequency over a 50 ms period for channel 20 from an L-mode plasma #26373, with the same DC signal level produced with an LED light source and from the un-illuminated sensor (electronic noise only).

A power spectrum $P(f)$ measured during an L-mode plasma discharge #26373 in an L-SND configuration with 900 kA plasma current and 1.8 MW NBI heating from the SS beam at 65 keV is shown in Figure 11. For comparison, the noise floor due to photon noise is also shown, which was measured by illuminating the sensor using the in-built calibration LED light source to produce the same DC signal level as during the plasma. It can be seen that the plasma fluctuation amplitude approaches the photon noise level at frequencies above ~100 kHz. The amplitude of the plasma fluctuations, which increases with decreasing frequency, is up to four orders of magnitude above the photon noise level. The overall SNR for the measurement is ~290 in this case, which is in agreement with the expected performance from the simulations. In this case the noise level from the electronics with the un-illuminated sensor at the same bias voltage as used for the plasma measurement is a factor ~5 below the photon noise level.

A spectrogram of the evolution of the cross-power as a function of frequency between two poloially separated channels (13 and 21) is shown in Figure 12 for an L-mode discharge #26069 with 1.4 MW of NBI heating at 60 keV energy, viewing at a location at mid-radius, $R_v \sim 1.2$ m. The period of NBI injection is from 0.04 to 0.32 s. During the initial stages of the discharge the outboard radius of the plasma R_{out} increases, passing the viewed radius at 0.08 s and reaching its maximum of 1.4 m at about 0.15 s. The initially high level of broadband turbulence up to 80 kHz is therefore from the periphery of the plasma. The higher frequency fluctuations from 80 kHz upwards at this time are due to toroidal Alfvén eigenmodes (TAEs) driven by the fast-ion pressure gradient.

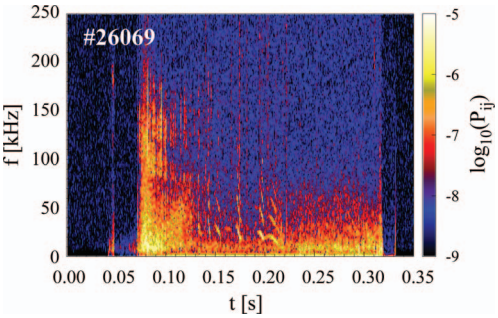

FIG. 12. (Color online) Spectrogram showing evolution of cross-power between channels 13 and 21 as a function of frequency during L-mode discharge #26069 with 1.4 MW of NBI heating at 60 keV beam energy when viewing at mid-radius at $Rv \sim 1.2$ m.

Some of the BE signal at the TAE frequency could be due to modulation of the FIDA contribution to the background intensity due to redistribution of the fast-ions by these modes. After 0.13 s the level of broadband turbulence at mid-radius is reduced, probably because of strong radial shear in the toroidal rotation in this region of the plasma. Between 0.13 and 0.22 s "fishbone" MHD modes, which are internal kink modes driven again by the fast-ion pressure gradient, can be seen with harmonics up to 80 kHz. After 0.2 s there is a low-n MHD mode which slows down and locks to the wall thereby reducing the toroidal rotation rate. In the subsequent period until the end of the discharge with low rotational shear the power of the broadband turbulence is almost an order of magnitude greater than in the earlier rotating phase prior to the mode locking.

VI. DISCUSSION

Initial results from the MAST BES turbulence imaging system show that the system performs as was expected from the simulations on which the design was based. The APD camera provides optimal SNR at the typical incident photon fluxes at the sensors of $\sim 10^{11}$ s^{-1}, which are achieved through the use of a high étendu, direct-coupled collection optics. The resulting SNR of ~300 allows for the detection of relative density fluctuations $\delta n_e/n_e$ of order 0.1% at frequencies of a few 100 kHz, which is typical of the amplitudes expected for ion-scale turbulence in the core of the spherical tokamak plasma. The spatial resolution achieved at mid-radius through the localisation of the emission to the beam of ~2–3 cm is sufficient for detection of ion scale turbulence with wavenumbers $k_{r,\theta} < 1.6\,\mathrm{cm}^{-1}$, i.e., with $k_{r,\theta}\rho_i < 1$. The initial results, including spectral measurements of the beam emission, showed that typically 5–10% of the detected signal is from background light, which is most likely localised to the plasma edge. Further spectral measurements performed through the BES optics allowed the origin of this background emission to be identified as D_α light leaking passed the interference filter. After masking out this light the background light level was reduced to only ~2% of the BE signal. Because fluctuation amplitudes at the plasma periphery can be an order of magnitude or more greater than in the core it remains a challenge to distinguish the core turbulence from the edge fluctuations. Comparison of data immediately before and after a cut-off of the NBI injection is a method to do this at least at one time in a discharge and modulation or short cuts of order 20 ms duration in the beam power would also be useful. Another feature of this data is the prevalence of coherent MHD activity at frequencies of a few kHz right up to the Nyquist frequency of 1 MHz. Power spectra show that the density perturbations from this activity, likely to be due to spatial perturbations of the equilibrium rather than actual density perturbations, are typically larger in magnitude than the broadband turbulence. It will be a challenge to develop a method to separate out the localised, ion-scale turbulence in the core plasma from this global, large scale MHD activity.

ACKNOWLEDGMENTS

This work was funded by the RCUK Energy Programme under grant EP/I-501045, the Hungarian National Development Agency under Contract No. NAP-1-2005-0013, and the European Communities under the contract of Association between EURATOM and CCFE and EURATOM HAS. The views and opinions expressed herein do not necessarily reflect those of the European Commission.

[1]X. Garbet, P. Mantica, C. Angioni, E. Asp, Y. Baranov, C. Bourdelle, R. Budny, F. Crisanti, G. Cordey, L. Garzotti, N. Kirneva, D. Hogeweij, T. Hoang, F. Imbeaux, E. Joffrin, X. Litaudon, A. Manini, D. C. McDonald, H. Nordman, V. Parail, A. Peeters, F. Ryter, C. Sozzi, M. Valovic, T. Tala, A. Thyagaraja, I. Voitsekhovitch, J. Weiland, H. Weisen, A. Zabolotsky, and the JET EFDA Contributors, Plasma Phys. Controlled Fusion **46**(12B), B557 (2004).
[2]A. J. Wootton, B. A. Carreras, H. Matsumoto, K. McGuire, W. A. Peebles, Ch. P. Ritz, P. W. Terry, and S. J. Zweben, Phys. Fluids B **2**, 2879 (1990).
[3]J. W. Connor and H. R. Wilson, Plasma Phys. Controlled Fusion **36**, 719 (1994).
[4]C. M. Roach, I. G. Abel, R. J. Akers, W. Arter, M. Barnes, Y. Camenen, F. J. Casson, G. Colyer, J. W. Connor, S. C. Cowley, D. Dickinson, W. Dorland, A. R. Field, W. Guttenfelder, G. W. Hammett, R. J. Hastie, E. Highcock, N. F. Loureiro, A. G. Peeters, M. Reshko, S. Saarelma, A. A. Schekochihin, M. Valovic, and H. R. Wilson, Plasma Phys. Controlled Fusion **51**, 124020 (2009).
[5]R. J. Fonck, P. A. Duperrex, and S. F. Paul, Rev. Sci. Instrum. **61**(11), 3487 (1990).
[6]S. Zoletnik, M. Anton, M. Endler, S. Fiedler, M. Hirsch, K. McCormick, and J. Schweinzer, Phys. Plasmas **6**, 4239 (1999).
[7]G. R. McKee, R. J. Fonck, D. K. Gupta, D. J. Schlossberg, M. W. Shafer, and R. L. Boivin, Rev. Sci. Instrum. **77**, 10F104 (2006).
[8]M. W. Shafer, G. R. McKee, M. E. Austin, K. H. Burrell, R. J. Fonck, and D. J. Schlossberg, Phys. Rev. Lett. **103**, 075004 (2009).
[9]D. K. Gupta, R. J. Fonck, G. R. McKee, D. J. Schlossberg, and M. W. Shafer, Phys. Rev. Lett. **97**, 125002 (2006).
[10]G. R. McKee, R. J. Fonck, D. K. Gupta, D. J. Schlossberg, M. W. Shafer, C. Holland, and G. Tynan, Rev. Sci. Instrum. **75**(10), 3490 (2004).
[11]C. Michael, K. Tanaka, L. Vyacheslavov, A. Sanin, K. Kawahata, and S. Okajima, Plasma Phys. Fusion Res. **2**, S1034 (2007).
[12]A. R. Field, D. Dunai, N. J. Conway, S. Zoletnik, and J. Sárközi, Rev. Sci. Instrum. **80**, 073503 (2009).
[13]N. J. Conway, P. G. Carolan, J. McCone, M. J. Walsh, and M. Wisse, Rev. Sci. Instrum. **77**, 10F131 (2006).
[14]Y. C. Ghim(Kim), A. R. Field, S. Zoletnik, and D. Dunai, Rev. Sci. Instrum. **81**, 10D713 (2010).
[15]I. G. Kiss, B. Meszaros, D. Dunai, S. Zoletnik, A. R. Field, and R. Gaffka, Fusion Eng. Des. **86**, 1315–1318 (2011).
[16]D. Dunai, S. Zoletnik, J. Sárközi, and A. R. Field, Rev. Sci. Instrum. **81**(1), 103503 (2010).